Powder Technology 429 (2023) 118954

Contents lists available at ScienceDirect

Powder Technology

journal homepage: www.journals.elsevier.com/powder-technology

Insight to evolution of particle size and penetration resistance of $Ca(OH)_2$/CaO powder bed for thermochemical energy storage

Yuxiang Cheng [a], Zhongjie Shen [a,*], Feng Lv [b], Dayang Wan [b], Yongchuan Gao [b], Yiru Yang [a], Haifeng Lu [a], Zhenghua Dai [a,*], Haifeng Liu [a]

[a] National Energy Coal Gasification Technology Research and Development Center and Shanghai Engineering Research Center of Coal Gasification, East China University of Science and Technology, P. O. Box 272, Shanghai 200237, PR China
[b] Luoyang Ruichang Environmental Engineering Co., Ltd., Luoyang 471027, PR China

HIGHLIGHTS

- Particle size and penetration resistance evolution of $Ca(OH)_2$/CaO bed was assessed.
- Sauter mean diameter increased and decreased during dehydration processes.
- Dehydration was found to cause a significant increase of penetration resistance.
- Particle size and penetration resistance of CaO bed remained a relative stability.

GRAPHICAL ABSTRACT

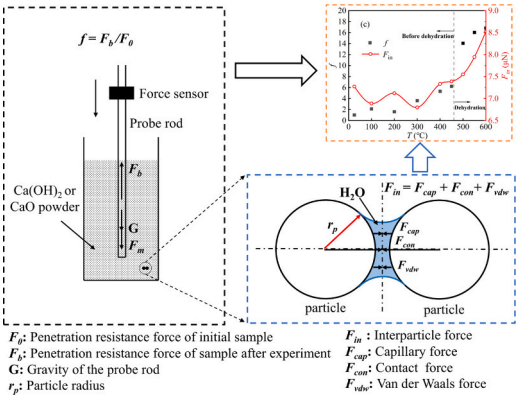

ARTICLE INFO

Keywords:
Thermochemical energy storage
$Ca(OH)_2$/CaO
Reaction cycle
Particle size distribution
Penetration resistance

ABSTRACT

During the $Ca(OH)_2$/CaO thermochemical energy storage process, the cyclability of reactions and the consolidation properties of powder storage are important issues to consider. In this study, experiments were conducted to assess the evolution of reaction conversion, particle size and penetration resistance of $Ca(OH)_2$/CaO powder fixed bed. The results revealed that the final conversions of both the hydration and dehydration reactions stabilized between 70 and 80%. The particle size distributions of $Ca(OH)_2$ increased initially and then decreased with the increasing cycle number and degree of dehydration. The dehydration conversion was the dominant factor for changing $Ca(OH)_2$ bed penetration resistance force. The particle size and penetration resistance of the CaO bed remained stable during long-term storage at high temperatures. The theoretical analysis of the interparticle forces agreed with the trend of the experimental results, with particle size and moisture content being the main factors affecting cohesion.

* Corresponding authors.
E-mail addresses: zjshen@ecust.edu.cn (Z. Shen), chinadai@ecust.edu.cn (Z. Dai).

https://doi.org/10.1016/j.powtec.2023.118954
Received 18 March 2023; Received in revised form 14 August 2023; Accepted 30 August 2023
Available online 1 September 2023

1. Introduction

Energy storage is one of the most promising schemes to effectively utilize renewable energy sources such as solar and geothermal energy [1]. In general, heat storage systems can be classified as sensible energy storage [2], latent energy storage [3], and thermochemical energy storage [4]. Among the various heat storage technologies, the $Ca(OH)_2$/CaO system is regarded as a prospective thermochemical energy storage system for high-temperature applications [5]. The heat storage and release process of the system is based on the reversible thermochemical reaction of $Ca(OH)_2$/CaO. Specifically, the dehydration reaction of $Ca(OH)_2$ absorbs heat to produce CaO and H_2O, while the hydration process of CaO releases heat, allowing $Ca(OH)_2$ to be regenerated. The system has several key advantages, including a high heat storage density, wide operating temperature range, and long-distance storage [6].

Experimental and theoretical investigations into the $Ca(OH)_2$/CaO system primarily focused on the kinetics of dehydration and hydration reaction [7–9], heat transfer enhancement [10], and the cyclability of the reaction system [11–15]. Research has shown that increasing the dehydration temperature results in an elevated charging rate during thermal storage [7,8]. The hydration process was found to be significantly affected by an increase in the partial pressure of water vapor [9]. The study also explored the influence of particle size on the intrinsic kinetics of the dehydration/hydration reaction, revealing a negative correlation between large particle sizes and reaction rate [11]. Additionally, investigations into the reaction cyclability demonstrated that an increase in the number of cycles and temperature can lead to sintering or agglomeration of particles, which can compromise the diffusion of water vapor and hinder the hydration process [12–15].

In the context of reactor selection for conducting dehydration and hydration reactions, the fixed bed reactor has traditionally been regarded as the research focus for the $Ca(OH)_2$/CaO system [16], compared to moving bed [17] and fluidized bed [18,19]. Nevertheless, fixed beds are associated with inherent limitations in terms of heat transfer efficiency. Due to their low thermal conductivity, fixed bed reactors require a sufficiently large heat transfer area. Moreover, during the hydration or dehydration process, a high-pressure drop is necessary within the reaction vessel to ensure that the particles are fully exposed to the reaction gas (H_2O) or protective gas [20,21]. Notably, the material type and particle size distribution can have a pronounced influence on multiple factors, including particle properties and bed properties (voidage and Sauter mean diameter), which in turn can significantly impact the pressure drop in the fixed bed [22,23]. During thermochemical cycles, the compositional changes of $Ca(OH)_2$/CaO mixtures can be assessed through conversion degree. In contrast, the evolution of particle size distribution in response to factors such as hydration-dehydration thermal cycles and temperature has received little attention in the literature.

In addition to the dehydration and hydration reactions, the intermittent nature of the energy storage process requires that $Ca(OH)_2$/CaO powders may be stored for varying durations. However, the storage process can lead to compaction/consolidation of the particles, which can cause problems or failures in industrial storage containers such as silos, bins, and hoppers [24]. Due to the combined effects of temperature and consolidation, the cohesion of powders can increase, resulting in higher-than-anticipated levels of cohesion in powders that are stored in containers at elevated temperatures [25]. Furthermore, cyclic variations in the temperature of the granular bed can lead to bed consolidation over time due to the thermo-mechanical coupling effect. It should be noted that the consolidation induced by temperature cannot be reversed by cooling the bed [26]. The consolidation properties of mixed materials under thermal cycling conditions are expected to differ from those of pure materials, but this phenomenon has not been fully investigated. In light of the factors discussed above, it is essential to investigate the effects of storage temperature, storage time, and conversion degree on the consolidation characteristics of the $Ca(OH)_2$/CaO bed during the thermochemical energy storage process.

Table 1
Chemical compositions of the samples.

Sample	Chemical composition/wt%				
ARCH	$Ca(OH)_2$ ≥ 95%	Fe ≤ 0.01%	Mg, alkali metals ≤0.5%	Sulfate ≤0.2%	Heavy metal ≤0.002%
ARCO	CaO ≥ 98%	Fe ≤ 0.015%	Mg, alkali metals ≤0.5%	Sulfate ≤0.2%	Heavy metal ≤0.005%

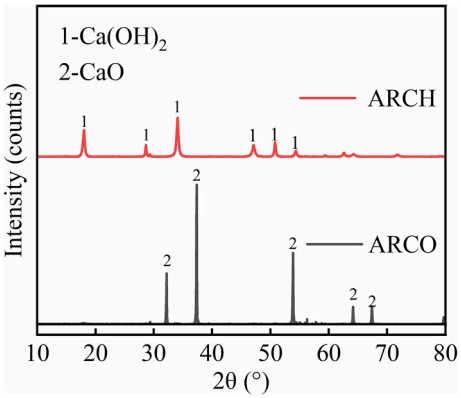

Fig. 1. XRD spectra of experimental samples in this study.

In this study, experiments were carried out to investigate the evolution of reaction conversion, particle size, and morphology after different numbers of cycles under conditions ensuring sufficient heat transfer and contact with reactive gases. The Sauter mean diameter was used to characterize the changes in particle size distribution. The effect of the dehydration reaction as well as storage temperature and time on the particle and consolidation properties of $Ca(OH)_2$/CaO was also analyzed using a static particle bed. The consolidation properties were assessed using the penetration resistance. Additionally, the inter-particle forces were calculated, and their correlation with penetration resistance was discussed.

2. Experimental

2.1. Materials

Two samples were used in this study for the experiments, which were $Ca(OH)_2$ powder (Analytical reagent, purity≥95 wt%, Shanghai Aladdin Biochemical Technology Co., Ltd., China) and CaO powder (Analytical reagent, purity≥98 wt%, Shanghai Aladdin Biochemical Technology Co., Ltd., China), respectively, which were denoted ARCH and ARCO in following sections. Their chemical compositions are shown in Table 1. The particle size distribution was measured by using a Camsizer XT (Verder Retsch Co., Ltd., Germany) laser light scattering instrument. The X-ray powder diffraction (XRD, PANalytical B.V., Netherlands) was carried out to determine the characteristic peaks of the sample. The particle size distribution and XRD analyses of two samples are shown in Fig. 1 and Fig. 2, respectively.

2.2. Experimental method

A high-temperature vertical tube furnace was used in this study. The schematic diagram of the experimental setup is shown in Fig. 3. The tube length was 1.0 m, and the isothermal temperature zone was located in the middle part of the furnace with a length of 30 cm. The experimental setup included a steam generator, temperature control system, heating furnace, and gas transport system. The heating tape was wrapped

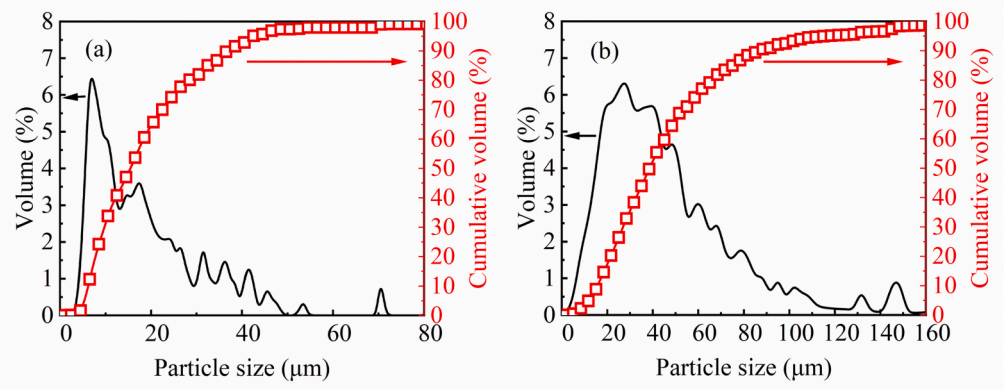

Fig. 2. Particle size distribution analysis of (a) ARCH, and (b) ARCO.

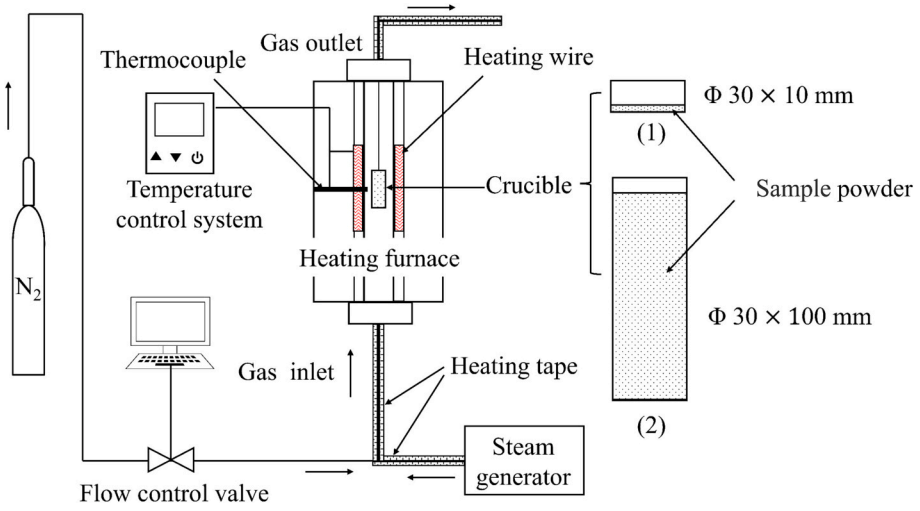

Fig. 3. Schematic diagram of the experimental setup.

around the furnace flange and gas pipeline to prevent the condensation of water vapor. Two types of crucibles were used in this study. Crucible (1) was used for the reaction cycle of $Ca(OH)_2/CaO$, and crucible (2) was used for the storage and penetration experiments. The material of both crucibles was aluminum oxide (purity 99.9%), and the specific dimensions are shown in Fig. 3.

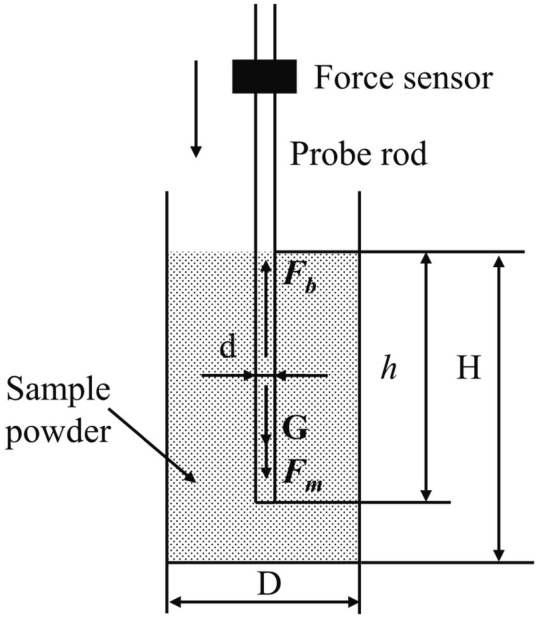

Fig. 4. Schematic diagram of force analysis.

Due to limitations in thermal conductivity, the localized temperature in the fixed-bed reaction zone can be non-uniform due to the endothermic and exothermic effects resulting from the dehydration/hydration reaction [27,28].To ensure proper contact with reactive gases and maximize heat transfer, the sample powder for the reaction cycle experiments was spread as a single layer of particles at the bottom of crucible (1). The sample mass of each experiment was controlled at approximately 0.2 g. Before each experiment, samples were dried in a dryer at 105 °C for 40 min to remove the moisture that was physically adsorbed on the sample. The furnace was subsequently heated to the setting temperature under a N_2 atmosphere. For the dehydration process, the setting temperature was 600 °C. After temperature stabilized, crucible (1) was placed down to the isothermal temperature zone. The N_2 flow rate was set at 150 mL/min and dehydration time is 10 min. The weight of crucible (1) containing the sample was measured both before and after the dehydration process. For the hydration process, the temperature was set to 400 °C, and the water vapor was introduced at a flow rate of 150 mL/min. The hydration time was also controlled at 10 min. The experiment then proceeded to the subsequent round of the dehydration process. In this study, the numbers of $Ca(OH)_2/CaO$ reaction cycles were set to 3, 10, and 20. The recorded mass changes were used to determine the conversion degrees of both the dehydration and hydration reactions. Furthermore, the microscopic morphology of the samples

before and after the reaction was analyzed via scanning electron microscopy (SEM, SU-1510, Hitachi, Ltd. Japan).

For the storage experiments, a crucible (2) was packed with a thick bed of bulk powdered samples to simulate the storage mode in the dense phase. When no reaction occurred (setting temperature ≤ 400 °C), the temperature of the sample within crucible (2) remained consistent with the setting temperature of the reactor. As previously mentioned, the temperature of the sample within crucible (2) had the potential to deviate from the setting temperature during the reaction process. The maximum temperature deviation was measured to be approximately 60–100 °C (setting temperature 400–600 °C). The initial height of the sample layer was the same in each experiment. Considering the variation in stacking density between calcium hydroxide and calcium oxide, the initial masses of the two samples were approximately 27 g and 40 g, respectively. The sample was then heated up to different temperatures and held on different storage time periods. The setting temperature for the storage experiment ranged from room temperature (25 °C) to 600 °C. The storage time period was set between 0 min and 10 h (600 min).

This study characterizes the consolidation properties of the bed by the penetration resistance [29,30] measured by a mechanical probe (Changzhou Allison Technology Co., LTD., measuring range 0–5 N, accuracy 0.05% F·S). The schematic diagram of the mechanical probe and force analytical principle are shown in Fig. 4. The bed accumulation height (H) is 90 mm, and the diameter of container (D) is 30 mm. The diameter of probe (d) is 5 mm. The probe is fixed on a vertical guide, the guide motion controls the distance and speed of movement. During measurements, the probe moves downward, and the tensile pressure sensor is used to measure the force as the probe penetrates the powder bed. The force sensor reading value is expressed as F_{m}, which can be obtained as $F_{\mathrm{m}} = F_b + \mathrm{G}$, where G is the gravity of the probe rod, F_b is the penetration resistance force of the sample powder. The experimental findings revealed a significant increase in the F_b when the ratio of the penetration depth (h) to the height of the bed (H) exceeded 0.9. This was attributed to the inherent length scale of interference arising from locally applied stress [30]. Consequently, the dimensionless resistance force f, which was defined as the ratio of penetration resistance of the sample after the experiment (F_b) to the penetration resistance of the initial sample (F_0) at the h/H of 0.9, was used in this study to quantify the consolidation degree under different conditions.

2.3. Dehydration and hydration efficiency

The reaction conversion degree X was calculated using Eq. (1).

$$X = \left(\frac{\Delta m}{\Delta m_{th}}\right)\cdot 100 = \left(\frac{m_0 - m_t}{M_{\mathrm{Ca(OH)_2}} - M_{CaO}}\frac{M_{\mathrm{Ca(OH)_2}}}{m_0 w_c}\right)\cdot 100 \tag{1}$$

Where Δm represents the instantaneous actual mass change, Δm_{th} is the theoretical mass change due to the dehydration reaction of $Ca(OH)_2$ in the sample. m_0 represent the initial sample mass, m_t is the sample mass at a point in the reaction, w_c is the mass fraction of $Ca(OH)_2$, $M_{\mathrm{Ca(OH)_2}}$ represents the molar mass of $Ca(OH)_2$, M_{CaO} is the molar mass of CaO molecules. The value of X ranges from 0 to 1. When X is equal to 0, the sample consists entirely of $Ca(OH)_2$, whereas when X is equal to 1, the entire sample is composed of CaO.

The conversion degree of the dehydration or hydration reaction in a given cycle is defined as ΔX_d and ΔX_h, which can be calculated by Eqs. (2) and (3), respectively.

$$\Delta X_d = X_d^f - X_d^0 \tag{2}$$

$$\Delta X_h = X_h^0 - X_h^f \tag{3}$$

Where X_d^0 and X_d^f denote the conversion degree of the sample at the start and end of the dehydration process in a given cycle, X_h^0 and X_h^f represent the conversion degree of the sample at the start and end of the hydration process in a given cycle.

Table 2
Parameters used in the calculation.

	ϵ [36–38]	n [39–41]
Calcium hydroxide	4.53	1.58
Calcium oxide	11.96	1.83
Nitrogen	1.000058	1.000 28

The particle size significantly affects the particle transmission process [31]. To evaluate the particle size distribution of samples under different conditions, the Sauter mean diameter D_{32} is introduced, which is expressed by Eq. (4).

$$D_{32} = \frac{\sum n_i d_i^3}{\sum n_i d_i^2} \tag{4}$$

To assess the variation in particle size during an experiment, the particle size change rate λ is defined. The equation is as follows:

$$\lambda = \frac{D_{32}^t - D_{32}^0}{D_{32}^0} \tag{5}$$

Where D_{32}^t is the Sauter mean diameter of the sample after the experiment, D_{32}^0 is the Sauter mean diameter of the initial sample.

2.4. Interparticle force prediction

The interparticle forces believed to be relevant to this study include Van der Waals forces, contact forces, and capillary forces. Van der Waals forces, although comparatively weaker than other types of interactions, play a critical role in all phenomena associated with intermolecular forces. Surface roughness exerts a pronounced impact on van der Waals forces, potentially inducing significant alterations in them [32]. The surface asperities r_{asp} can be calculated by [33]:

$$r_{asp} \sim \left(r_p z_0^2\right)^{1/3} \tag{6}$$

The total van der Waals force equation according to Rumpf's model can be expressed as [34]:

$$F_{vdw} = \frac{A}{12 z_0^2}\left[\frac{d_{asp} D}{d_{asp} + D} + \frac{D}{\left(1 + d_{asp}/(2z_0)^2\right)}\right] \tag{7}$$

Where A is the Hamaker constant, D is the particle diameter, represented by the value D_{32} in this study, d_{asp} is the surface asperity diameter, r_p is the particle radius, z_0 is the minimum interparticle separation distance, $z_0 = 0.4$ nm. The Hamaker constant can be calculated in different ways. The method to compute the Hamaker constant presented by Israelachvili [35] is:

$$A = \frac{3}{4} kT\left(\frac{\epsilon_a - \epsilon_b}{\epsilon_a + \epsilon_b}\right)^2 + \frac{3 h \nu_e}{16\sqrt{2}}\frac{\left(n_a^2 - n_b^2\right)^2}{\left(n_a^2 + n_b^2\right)^{3/2}} \tag{8}$$

where ϵ_a and ϵ_b are the static dielectric constants of the particle and the gas respectively and n_a and n_b are the refractive indices. ν_e is the main electronic absorption frequency, typically around $3 \times 10^{15}\ s^{-1}$. The values of the parameters used in the calculations are shown in Table 2.

For contact between two identical elastic solid spheres, the adhesion or pull-off force can be calculated by the Johnson-Kendall-Roberts (JKR) approximation, particularly in cases of highly deformable contacts or cases of high surface energy, large particles, and low elastic modulus. The contact force can be calculated by the following Eq. [42].

$$F_{\mathrm{con}} \approx \pi r_p^2 \gamma_{sv} \Big/ 2 r_p \tag{9}$$

where γ_{sv} is the solid-vapor interfacial energy, for $Ca(OH)_2$ the value is 1.18 N/m, for CaO is 1.11 N/m [43], r_p is the particle radius.

Capillary forces are generated by the formation of 'liquid bridges'

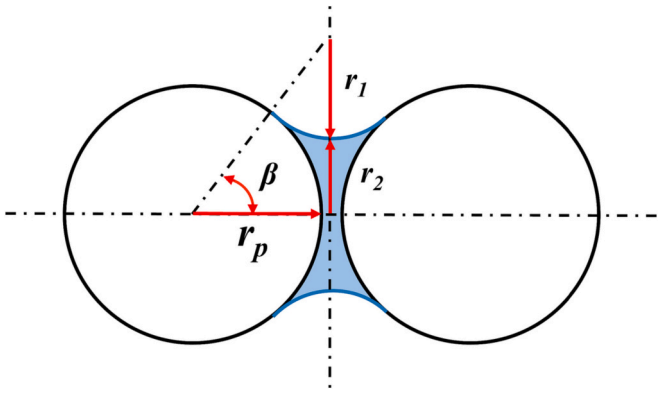

Fig. 5. The sketch of the liquid bridge geometry.

through movable liquid films at interparticle contact points. The sketch of the liquid bridge geometry is shown in Fig. 5. The presence of suitable vapor in the surrounding gas at a sufficiently high partial pressure can also cause condensation, resulting in the generation of liquid bridges. Seville et al. [44] derived the formula for the capillary force F_{cap} as:

$$F_{cap} = \gamma_L \pi r_2 \frac{r_1 + r_2}{r_1} = \frac{\gamma \pi r_p}{1 + tan\frac{\beta}{2}} \tag{10}$$

where the surface tension for the water (γ_L) is 72.8 × 10^{-3} N/m. The half-filling bridge angle (β)is related to the moisture content, i. e. relative humidity (RH) [45].

In addition, the interparticle force is defined as F_{in}, which is the sum of the above cohesive force.

$$F_{in} = F_{vdw} + F_{con} + F_{cap} \tag{11}$$

3. Results and discussion

3.1. Dehydration/hydration reaction cycle

Reaction cycle experiments were conducted to evaluate the cyclability of the $Ca(OH)_2$/CaO thermochemical energy storage system, using ARCH as the initial sample. The experimental configuration used the crucible (1). The dehydration and hydration reaction conversion degrees at the different cycle numbers are shown in Fig. 6. The results revealed that the dehydration and hydration reaction conversion declined with increasing the number of reaction cycles. The first cycle had the highest conversion value of about 98.2%. The reaction conversion was decreased by 5.29% for dehydration and 11.2% for hydration after 3 cycles, and eventually settled at about 78.6% after 20 cycles. Meanwhile, the hydration reaction conversion diminished to 70.5% after 20 cycles. The rehydration rate exhibits a decline with an increasing number of dehydration processes, which can be attributed to agglomeration and the reduction in pore volume and specific surface area, consequently diminishing the vapor diffusivity [12].

Fig. 7 shows SEM images of the samples following different cycle numbers. It can be observed that the majority of the initial samples were loose and composed of small-sized powders. However, the samples after 3 and 10 cycles exhibited a significant increase in large-sized powders (> 100 μm). Subsequently, after 20 cycles, the sample was once again dominated by small particles.

3.2. Effect of reaction cycle number on particle size distribution

Particle size distribution is a critical factor that can significantly impact the reaction rate [46]. Fig. 8 shows the particle size distribution and Sauter mean diameter (D_{32}) of the ARCH sample after different reaction cycles using the crucible (1). The results indicated that the proportion of large particles in the sample after reaction cycles was higher than that of the initial ARCH sample. The results in Fig. 8b demonstrated that D_{32} initially increased to 21.37 μm after 10 cycles and then dropped to 14.39 μm after 20 cycles. After 3 cycles, the particle size change rate λ was 14.31%, 50.59% after 10 cycles, and 1.41% after 20 cycles. The increase of particle size was related to the formation of CaO by dehydration reaction, while the decrease of particle size was related to particle sintering [47].

3.3. Particle size variation at different dehydration conversion

Due to the changes of substances during the dehydration process of $Ca(OH)_2$, as well as the escape of water vapor, the variations in its particle size distribution may be quite drastic and complex. The changes in cumulative particle size distribution of ARCH powders at different dehydration conversion degrees in the first reaction cycle using the crucible (2) are shown in Fig. 9. With the increase in dehydration conversion, the proportion of large particles rose and then dropped, as revealed by the evolution of the cumulative particle size distribution. The D_{32} initially increased and then decreased, reaching its maximum value 29.73 μm at 55% dehydration conversion, as shown in Fig. 9b. The maximum λ was 109.51%. When reached 99% dehydration conversion, λ dropped to −1.55%. The results revealed that particle agglomerated during dehydration and then shrank or fragmented into smaller particles when conversion increased.

3.4. Effect of storage temperature and time period on particle size evolution

The ARCH and ARCO samples were stored in crucible (2) at varying temperatures (100, 200, 300, 400, 500, and 600 °C) for 10 min. The results are shown in Fig. 10. Fig. 10a showed that the cumulative volume

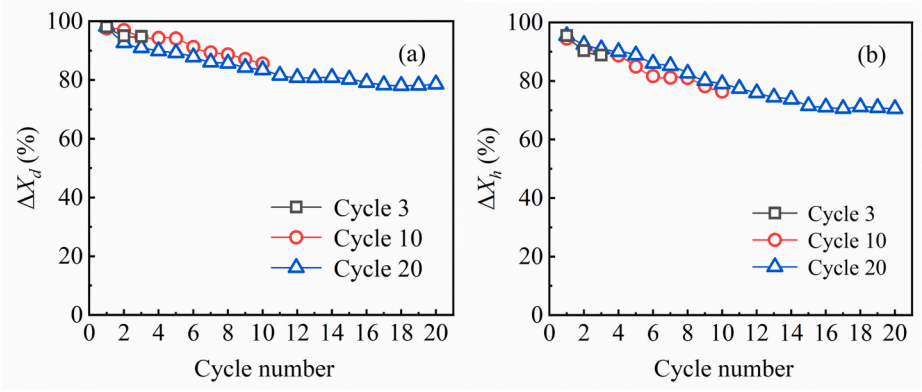

Fig. 6. (a) Dehydration and (b) hydration conversion degrees at the different cycle numbers.

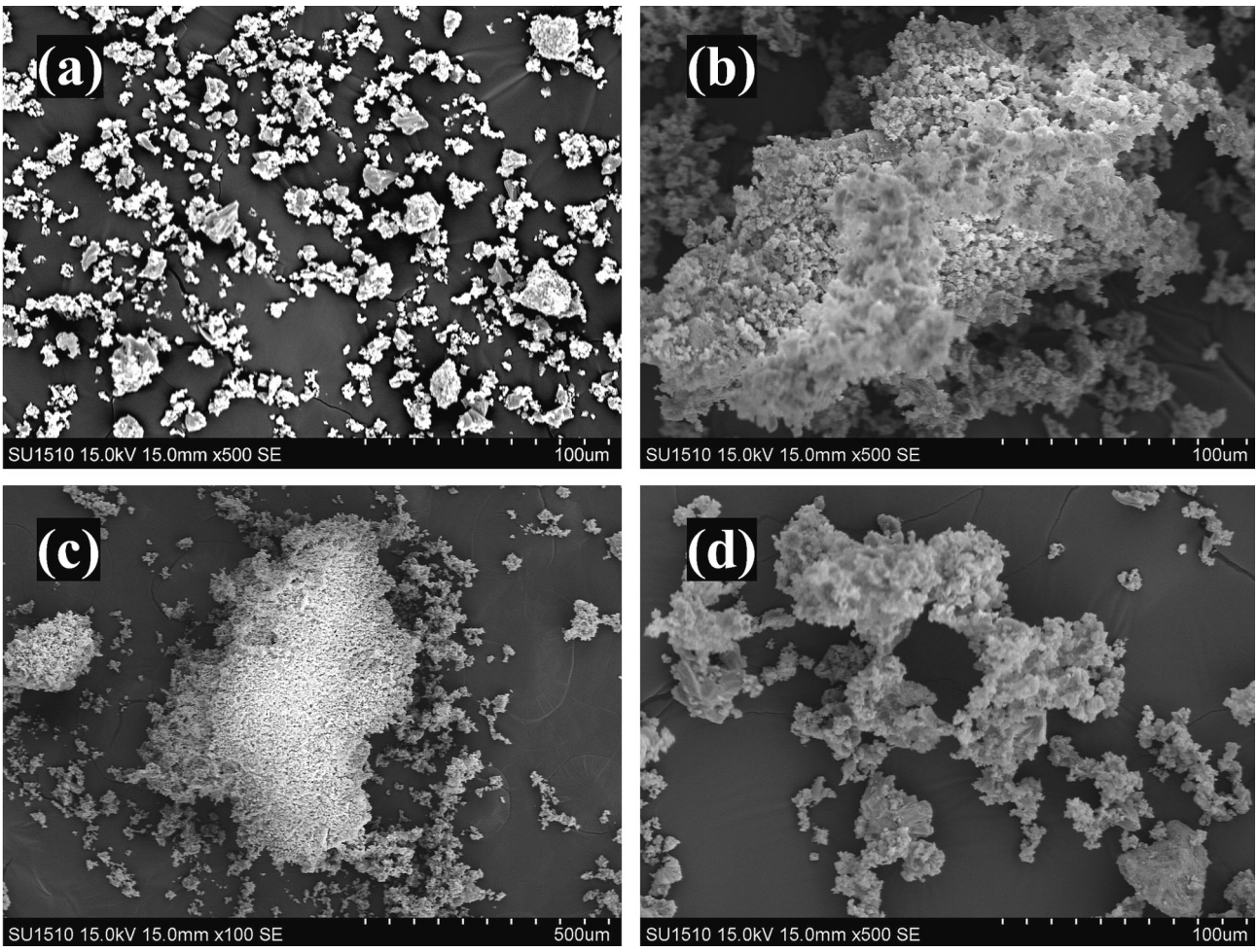

Fig. 7. SEM images of samples after different number of reaction cycles. (a) ARCH-initial, (b) 3 cycles, (c) 10 cycles, (d) 20 cycles.

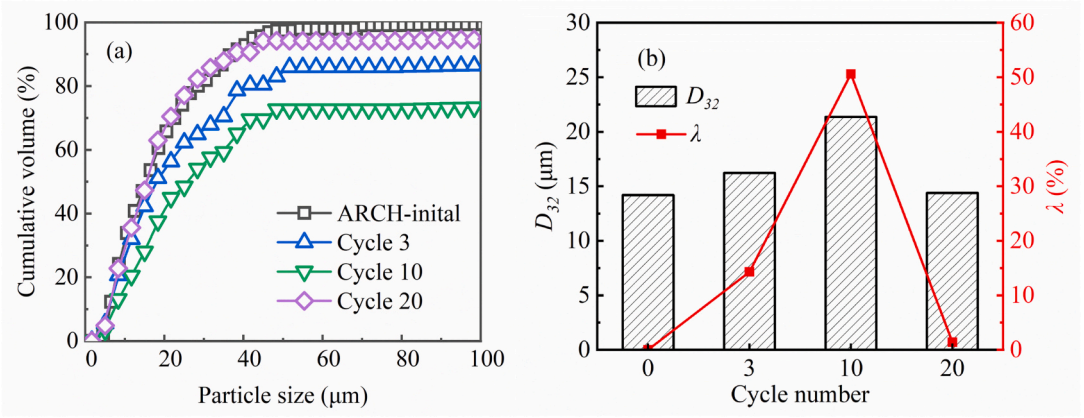

Fig. 8. (a) The cumulative particle size distribution, (b) Sauter mean diameter D_{32} and the particle size change rate (λ) of ARCH at different reaction cycles.

of large particle size for ARCH oscillated with storage temperature, particularly at 600 °C. In contrast, the cumulative volume of large particle size for ARCO diminished with the increase in storage temperature, as revealed by the results in Fig. 10b. As shown in Fig. 10c, the D_{32} for ARCH declined initially within a fluctuation value of 0 to −7% when the temperature rose from 100 to 400 °C. When the temperature increased to 600 °C, D_{32} for ARCH ascended to 16.24 μm and λ rose to 14.44%. Below the dehydration temperature, $Ca(OH)_2$ will result in a reduction of particle size on a micrometer level. Conversely, the D_{32} of ARCO remained relatively stable at temperatures ranging from 25 to 600 °C, as indicated by a maximum λ below 3%. In conclusion, the results of Fig. 10 suggested that the particle size distribution of $Ca(OH)_2$/CaO powders will remain relatively stable during a short-term storage process below 500 °C.

Fig. 11 shows the particle size distributions for ARCO at various storage time period intervals at 400 °C, using crucible (2) as the experimental configuration. The results revealed that the particle size diminished initially when the storage time period was shorter than 120

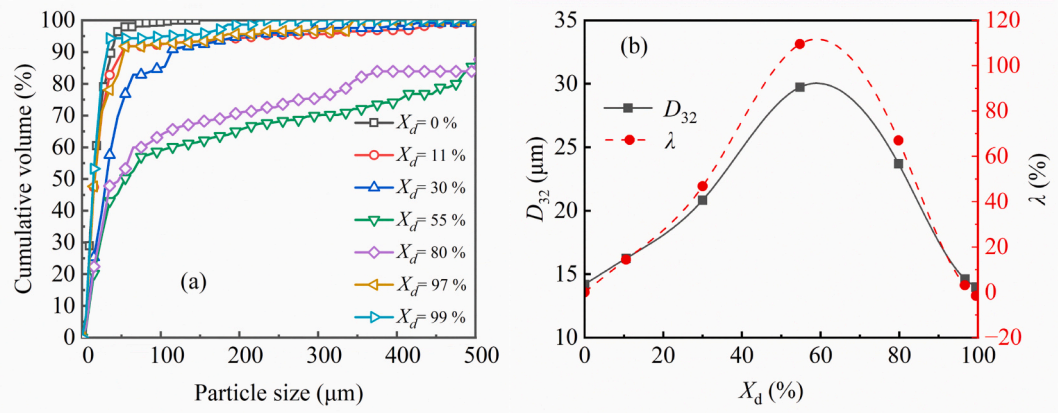

Fig. 9. Evolutions of (a) the cumulative particle size distribution, (b) Sauter mean diameter D_{32} and the particle size change rate (λ) at different dehydration conversions (X_d) in the first reaction cycle.

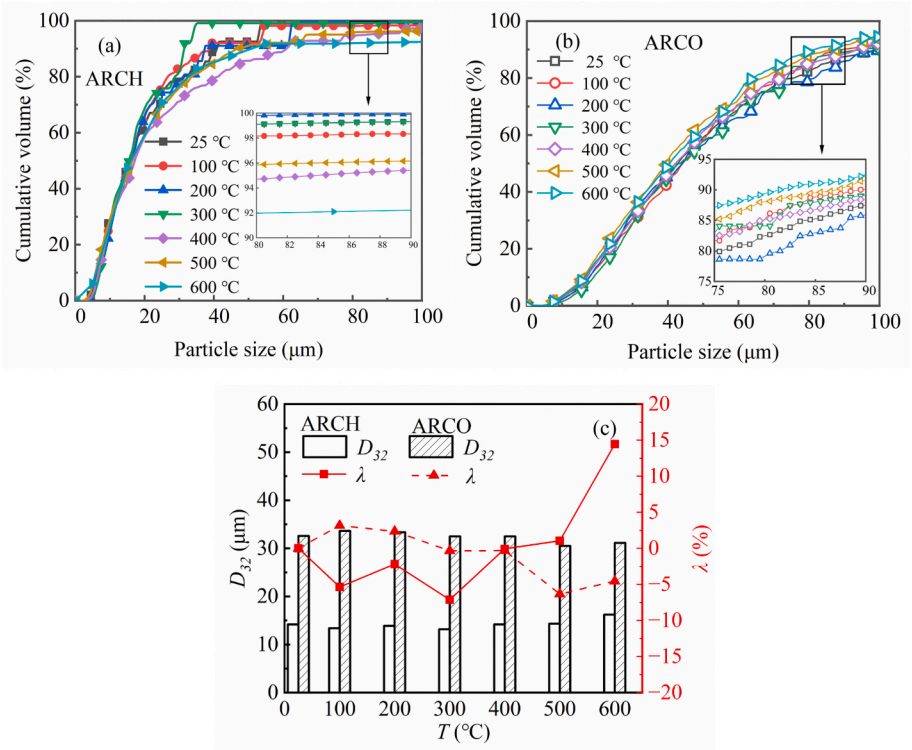

Fig. 10. The cumulative particle size distribution of (a) ARCH and (b) ARCO, and (c) comparisons of Sauter mean diameter (D_{32}) and particle size change rate (λ) at different temperatures (T = 100, 200, 300, 400, 500, and 600 °C).

min. The initial value of D_{32} was 33 μm and then declined to 30.5 μm when the storage time period was 60 min. The λ varied from 0 to −10%. Increasing the storage time period had a minor influence on the particle size distribution of ARCO.

3.5. Interparticle cohesive forces and penetration resistance

Theoretical analysis of the inter-particle forces can serve as an effective method to indicate changes in the pull-off force between particles when there are variations in particle characteristics or external conditions. This allows for an estimation of the degree of powder cohesiveness. [48]. Fig. 12 compared the calculated interparticle cohesive forces with the gravity of a calcium hydroxide particle based on the Eqs. (6)–(11). As shown in Fig. 12, the contact force calculated by JKR approximation has the most significant magnitude. The results demonstrated that the van der Waals force and gravity have the same magnitude at a particle size of approximately 45 μm. The D_{32} range in this study was between 10 and 40 μm, indicating that van der Waals forces have a notable effect on the particles. Moreover, the existence of moisture content in calcium hydroxide after dehydration may lead to capillary forces.

Interparticle cohesive forces is typically associated with both temperature and consolidation [25]. To assess consolidation characteristic, it is essential to perform quantitative tests with macroscopic experiments. The results of F_b of ARCH at different temperatures (25–600 °C) using the crucible (2) as sample containers are shown in Fig. 13. A slight increase in F_b was observed with the temperature increasing. ARCH underwent a dehydration reaction at temperatures above 500 °C. The F_{in} also exhibited a trend of increasing values with rising temperature. As the temperature increases to 500 °C, the penetration resistance force (F_b)

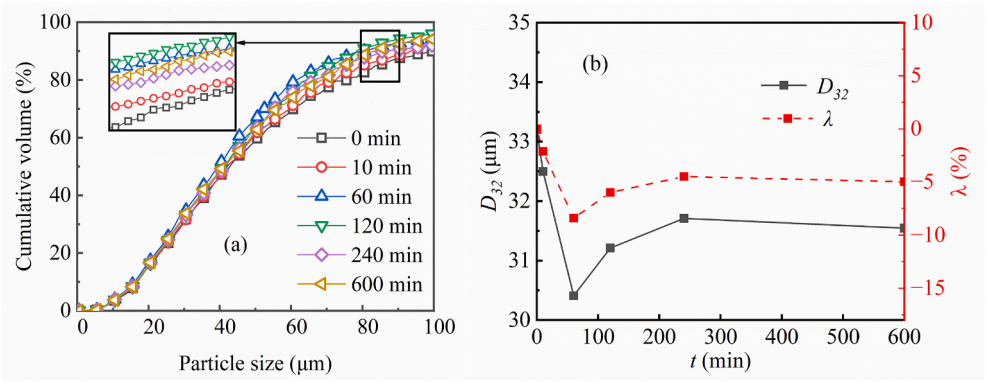

Fig. 11. (a) The cumulative particle size distribution, (b) Sauter mean diameter (D_{32}) and particle size change rate (λ) of ARCO sample at different storage time periods (0, 10, 20, 120, 240, 600 min) at 400 °C.

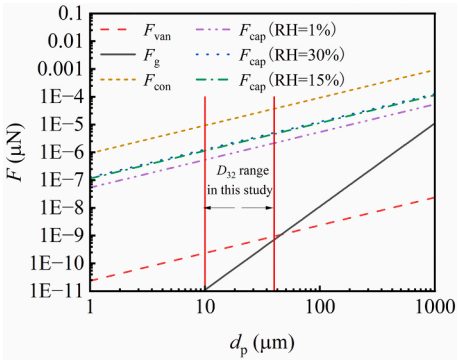

Fig. 12. Comparison of calculated values of interparticle forces and the gravity of calcium hydroxide particle. Red line means the range of D_{32} in this study. (For interpretation of the references to colour in this figure legend, the reader is referred to the web version of this article.)

nearly doubles compared to the temperature range of 25–450 °C. However, in the temperature range where the dehydration reaction occurred (500–600 °C), the effect of increasing reactor temperature on the penetration resistance became less significant, which differed from the situation when no dehydration reaction occurred. Under conditions of low thermal conductivity in a fixed-bed system, the heat absorption effect of the dehydration reaction may cause the temperature of the particle bed to decrease locally (especially in the central region) [27,28]. This phenomenon ultimately led to a reduced sensitivity of the penetration resistance to the reactor temperature within the range of 500–600 °C.

The F_b of ARCH at different dehydration conversions (X_d) were measured using the crucible (2), as demonstrated in Fig. 14. As the dehydration reaction progressed, the penetration resistance force (F_b) at a given h/H increased and reached its maximum value at a dehydration conversion degree of $X_d = 55\%$. The dehydration reaction of the calcium hydroxide bed significantly amplified the degree of consolidation. Nevertheless, a partial alleviation of bed consolidation was observed upon completion of the dehydration process. During the dehydration reaction, water vapor is generated and diffused. However, the low diffusion efficiency within the fixed bed can result in moisture accumulation. As shown in Fig. 12, even a slight moisture content can have a significant impact on interparticle forces. During the dehydration reaction, the moisture content and particle size initially increased and then gradually decreased, leading to changes in interparticle forces. This ultimately resulted in the initial increase and subsequent decrease in penetration resistance.

Additionally, whether the storage process of calcium oxide powder triggers the consolidation of powder beds needs to be examined. Fig. 15 illustrated the variation of the penetration resistance force, F_b, and dimensionless resistance force, f, of the ARCO bed at different temperatures. The experiments were conducted with the crucible (2). As shown in Fig. 15a, F_b rose with the increasing storage temperature and h/H. At temperatures above 400 °C, the penetration resistance increased more significantly with rising temperature. The maximum value of f was 6.9 at the temperature of 600 °C, which was smaller than that of the ARCH bed. The results showed that the trends of F_{in} and f are inconsistent at 500–600 °C. However, given that the changes of and f are relatively small, the inconsistency is acceptable.

Fig. 16 shows the results of the effect of the storage time period on the penetration resistance force (F_b), dimensionless resistance force (f), and interparticle force (F_{in}). The experiments were also performed using the crucible (2). The F_b of the ARCO bed increased with prolonged storage time period and h/H. Both the calculated value F_{in} and the experimental value f have a tendency to increase with the increase of the storage time and finally stabilize. This indicated that prolonged storage time of a pure CaO bed will promote consolidation, but the extent of consolidation will not continue to increase indefinitely. There was likely to be a threshold beyond which the bed will stabilize and further consolidation will not occur. Based on the experimental results presented in Figs. 10, 11, 15, and 16, it can be concluded that calcium oxide powder was more suitable for prolonged storage at high temperatures, as it exhibited less particle size variation and more stable consolidation properties.

4. Conclusions

This study investigated the effects of reaction cycle number, reaction conversion, storage temperature, and time on the variation of particle size distribution and bed penetration resistance force of the $Ca(OH)_2$/CaO thermochemical energy storage process. The results of the reaction cycle experiments showed that the particle size distribution of $Ca(OH)_2$ powders initially increased and then decreased with the reaction cycle number and dehydration conversion degree. The D_{32} value of $Ca(OH)_2$ powder exceeded twice the initial sample's value at a dehydration conversion degree of 55%. In contrast, the D_{32} value of CaO powder showed only minor changes as storage temperature or time increased, with change rates remaining below 10%. The penetration resistance of $Ca(OH)_2$ and CaO increased with the storage temperature and time, particularly for $Ca(OH)_2$. Dehydration conversion degree was founded to be a dominant factor in changing the penetration resistance of the $Ca(OH)_2$ bed. Below the dehydration temperature, the influence of temperature was limited. The CaO was found to consolidation when stored at temperatures higher than 400 °C, with a rapid increase in penetration resistance force followed by stabilization over a short storage time. The calculated interparticle forces agreed with the trend of the experimental

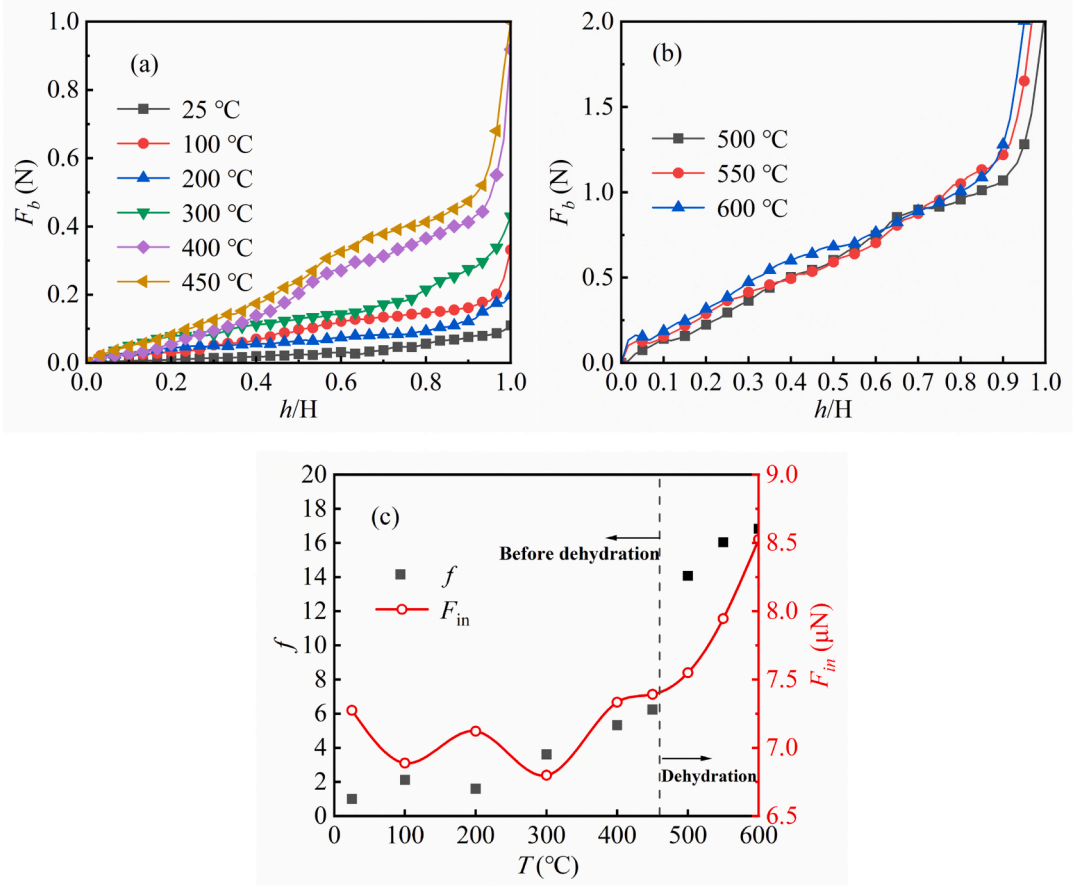

Fig. 13. Variation of the penetration resistance force F_b, the dimensionless resistance force f of ARCH bed, and calculated interparticle force value F_{in} at different temperatures (25–600 °C).

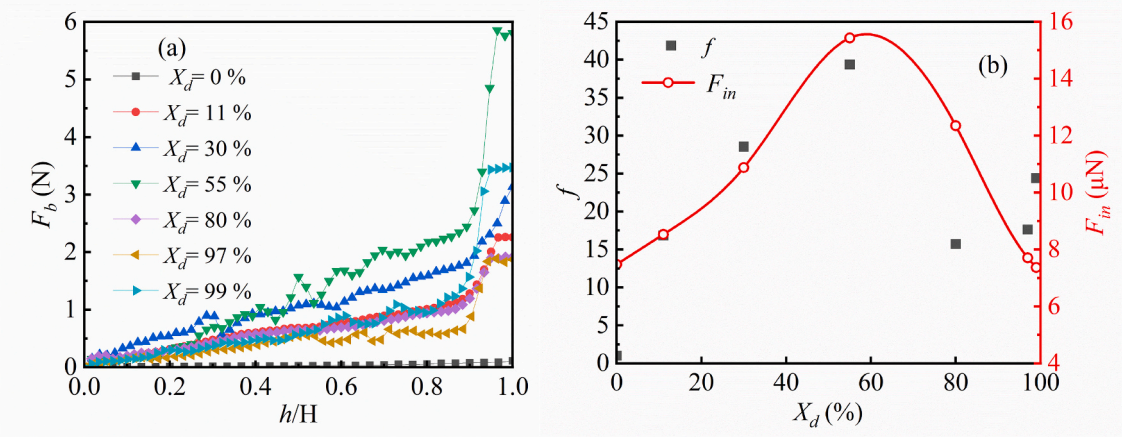

Fig. 14. Variation of (a) the penetration resistance force F_b with the relationship of h/H, (b) dimensionless resistance force f of ARCH bed, and calculated interparticle force value F_{in} at different dehydration conversions (X_d).

results of the penetration resistance experiment, revealing the dominant effect of particle size and moisture content on adhesion. This study has provided valuable insight and guidance into the reaction cycle process and storage process of $Ca(OH)_2$/CaO-based thermal chemical energy storage.

CRediT authorship contribution statement

Yuxiang Cheng: Resources, Data curation, Formal analysis, Investigation, Methodology, Software, Visualization, Writing – original draft, Writing – review & editing. **Zhongjie Shen:** Conceptualization, Supervision, Formal analysis, Methodology, Software, Writing – original draft, Writing – review & editing, Project administration, Funding acquisition. **Feng Lv:** Resources, Data curation, Formal analysis, Investigation, Methodology, Software, Visualization, Writing – review & editing. **Dayang Wan:** Resources, Data curation, Formal analysis, Investigation, Methodology, Software, Visualization, Writing – review & editing. **Yongchuan Gao:** Resources, Data curation, Formal analysis,

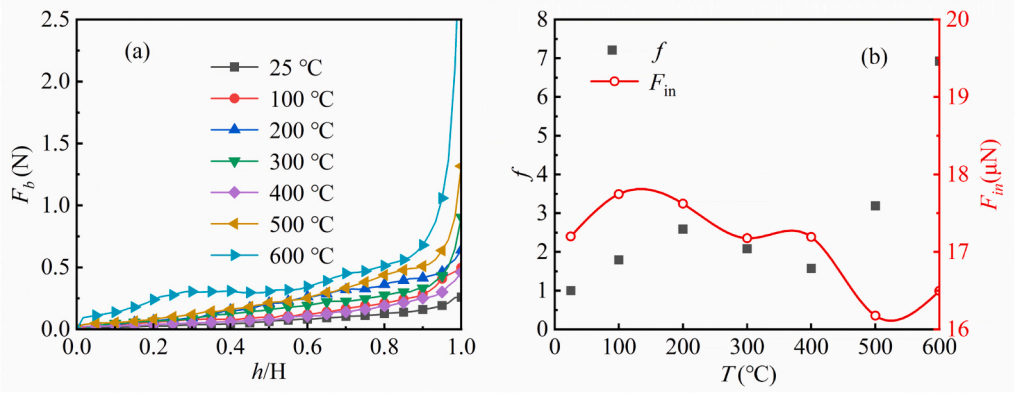

Fig. 15. Variation of (a) the penetration resistance force F_b with the relationship of h/H, (b) dimensionless resistance force f of ARCO bed, and calculated inter-particle force value F_{in} at different temperatures.

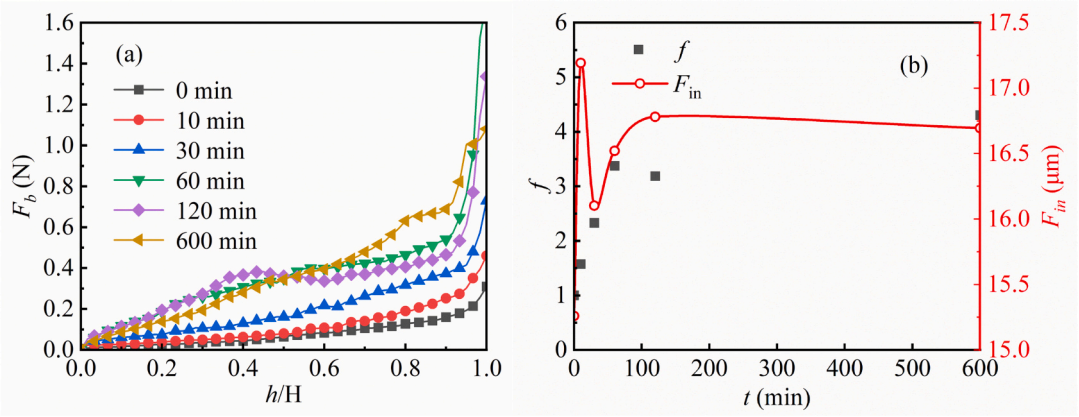

Fig. 16. Variation of (a) the penetration resistance force F_b with the relationship of h/H, (b) dimensionless resistance force f of ARCO bed, and calculated inter-particle force value F_{in} at different storage time periods at 400 °C.

Investigation, Methodology, Software, Visualization, Writing – review & editing. **Yiru Yang:** Conceptualization, Resources, Data curation, Formal analysis, Software, Writing – original draft, Writing – review & editing. **Haifeng Lu:** Validation, Resources, Investigation, Methodology, Writing – review & editing. **Zhenghua Dai:** Conceptualization, Supervision, Formal analysis, Methodology, Software, Writing – original draft, Writing – review & editing. **Haifeng Liu:** Conceptualization, Supervision, Validation, Formal analysis, Methodology.

Declaration of Competing Interest

The authors declare that they have no known competing financial interests or personal relationships that could have appeared to influence the work reported in this paper.

Data availability

The authors do not have permission to share data.

Acknowledgements

This study is supported by the National Key R&D Program of China (2022YFC3902502-04), the Shanghai Pujiang Program (21PJ1402300), Key R&D Program of Xinjiang Uygur Autonomous Region (2022B03026-1), the Fundamental Research Funds of the Central Universities (2022ZFJH004 and JKB01221677).

References

[1] A. Bayon, R. Bader, M. Jafarian, L. Fedunik-Hofman, Y. Sun, J. Hinkley, S. Miller, W. Lipiński, Techno-economic assessment of solid–gas thermochemical energy storage systems for solar thermal power applications, Energy. 149 (2018) 473–484, https://doi.org/10.1016/j.energy.2017.11.084.
[2] B. Koçak, A.I. Fernandez, H. Paksoy, Review on sensible thermal energy storage for industrial solar applications and sustainability aspects, Sol. Energy 209 (2020) 135–169, https://doi.org/10.1016/j.solener.2020.08.081.
[3] Z. Li, Y. Lu, R. Huang, J. Chang, X. Yu, R. Jiang, X. Yu, A.P. Roskilly, Applications and technological challenges for heat recovery, storage and utilisation with latent thermal energy storage, Appl. Energy 283 (2021), 116277, https://doi.org/10.1016/j.apenergy.2020.116277.
[4] M.I. Khan, F. Asfand, S.G. Al-Ghamdi, Progress in research and technological advancements of thermal energy storage systems for concentrated solar power, J. Energy Storage 55 (2022), 105860, https://doi.org/10.1016/j.est.2022.105860.
[5] A.J. Carrillo, J. González-Aguilar, M. Romero, J.M. Coronado, Solar energy on demand: a review on high temperature thermochemical heat storage systems and materials, Chem. Rev. 119 (2019) 4777–4816, https://doi.org/10.1021/acs.chemrev.8b00315.
[6] P. Pardo, A. Deydier, Z. Anxionnaz-Minvielle, S. Rougé, M. Cabassud, P. Cognet, A review on high temperature thermochemical heat energy storage, Renew. Sust. Energ. Rev. 32 (2014) 591–610, https://doi.org/10.1016/j.rser.2013.12.014.
[7] X.F. Long, L. Dai, B. Lou, J. Wu, The kinetics research of thermochemical energy storage system Ca(OH)2/CaO, Int. J. Energy Res. 41 (2017) 1004–1013, https://doi.org/10.1002/er.3688.
[8] J. Yan, C.Y. Zhao, B.Q. Xia, T. Wang, The effect of dehydration temperatures on the performance of the CaO/Ca(OH)2 thermochemical heat storage system, Energy. 186 (2019), 115837, https://doi.org/10.1016/j.energy.2019.07.167.
[9] Y.A. Criado, M. Alonso, J.C. Abanades, Kinetics of the CaO/ca(OH)2 hydration/dehydration reaction for thermochemical energy storage applications, Ind. Eng. Chem. Res. 53 (2014) 12594–12601, https://doi.org/10.1021/ie404246p.
[10] Q. Ranjha, A. Oztekin, Numerical analyses of three-dimensional fixed reaction bed for thermochemical energy storage, Renew. Energy 111 (2017) 825–835, https://doi.org/10.1016/j.renene.2017.04.062.

[11] J. Yan, C.Y. Zhao, Experimental study of CaO/Ca(OH)2 in a fixed-bed reactor for thermochemical heat storage, Appl. Energy 175 (2016) 277–284, https://doi.org/10.1016/j.apenergy.2016.05.038.
[12] C. Huang, M. Xu, X. Huai, Synthesis and performances evaluation of the spindle-shaped calcium hydroxide nanomaterials for thermochemical energy storage, J. Nanopart. Res. 21 (2019) 262, https://doi.org/10.1007/s11051-019-4694-z.
[13] C. Roßkopf, M. Haas, A. Faik, M. Linder, A. Wörner, Improving powder bed properties for thermochemical storage by adding nanoparticles, Energy Convers. Manag. 86 (2014) 93–98, https://doi.org/10.1016/j.enconman.2014.05.017.
[14] M. Xu, X. Huai, J. Cai, Agglomeration behavior of calcium hydroxide/calcium oxide as thermochemical heat storage material: a reactive molecular dynamics study, J. Phys. Chem. C 121 (2017) 3025–3033, https://doi.org/10.1021/acs.jpcc.6b08615.
[15] L. Dai, X.-F. Long, B. Lou, J. Wu, Thermal cycling stability of thermochemical energy storage system Ca(OH)2/CaO, Appl. Therm. Eng. 133 (2018) 261–268, https://doi.org/10.1016/j.applthermaleng.2018.01.059.
[16] M. Schmidt, A. Gutierrez, M. Linder, Thermochemical energy storage with CaO/Ca(OH)2 – experimental investigation of the thermal capability at low vapor pressures in a lab scale reactor, Appl. Energy 188 (2017) 672–681, https://doi.org/10.1016/j.apenergy.2016.11.023.
[17] A. Cosquillo Mejia, S. Afflerbach, M. Linder, M. Schmidt, Experimental analysis of encapsulated CaO/Ca(OH)2 granules as thermochemical storage in a novel moving bed reactor, Appl. Therm. Eng. 169 (2020), 114961, https://doi.org/10.1016/j.applthermaleng.2020.114961.
[18] K. Risthaus, M. Linder, M. Schmidt, Experimental investigation of a novel mechanically fluidized bed reactor for thermochemical energy storage with calcium hydroxide/calcium oxide, Appl. Energy 315 (2022), 118976, https://doi.org/10.1016/j.apenergy.2022.118976.
[19] C. Tregambi, M. Troiano, F. Montagnaro, R. Solimene, P. Salatino, Fluidized beds for concentrated solar thermal technologies—a review, Front. Energy Res. 9 (2021), https://doi.org/10.3389/fenrg.2021.618421.
[20] I. Fujii, K. Tsuchiya, M. Higano, J. Yamada, Studies of an energy storage system by use of the reversible chemical reaction: CaO + H2O ⇌ Ca(OH)2, Sol. Energy 34 (1985) 367–377, https://doi.org/10.1016/0038-092X(85)90049-0.
[21] A. Kanzawa, Y. Arai, Thermal energy storage by the chemical reaction augmentation of heat transfer and thermal decomposition in the CaO/Ca(OH)2 powder, Sol. Energy 27 (1981) 289–294, https://doi.org/10.1016/0038-092X(81)90061-X.
[22] A. Koekemoer, A. Luckos, Effect of material type and particle size distribution on pressure drop in packed beds of large particles: extending the Ergun equation, Fuel. 158 (2015) 232–238, https://doi.org/10.1016/j.fuel.2015.05.036.
[23] X. Luo, L. Zhao, M. Zhang, H. Dong, DEM study on the effects of pellet characteristics on particle flow in rectangular hopper, Powder Technol. 373 (2020) 476–487, https://doi.org/10.1016/j.powtec.2020.06.027.
[24] E. Teunou, J.J. Fitzpatrick, Effect of storage time and consolidation on food powder flowability, J. Food Eng. 43 (2000) 97–101, https://doi.org/10.1016/S0260-8774(99)00137-5.
[25] F.J. Durán-Olivencia, M.J. Espín, J.M. Valverde, Cross effect between temperature and consolidation on the flow behavior of granular materials in thermal energy storage systems, Powder Technol. 363 (2020) 135–145, https://doi.org/10.1016/j.powtec.2019.11.125.
[26] A.F. Alenzi, Modeling of Consolidation and Flow of Granular Material under Varying Conditions, University of Pittsburgh, 2012.
[27] M. Wang, L. Chen, Y. Zhou, W.Q. Tao, Numerical simulation of the physical–chemical–thermal processes during hydration reaction of the calcium oxide/calcium hydroxide system in an indirect reactor, Transp. Porous Media 140 (2021) 667–696, https://doi.org/10.1007/s11242-020-01514-w.
[28] M. Wang, L. Chen, Y. Zhang, W.Q. Tao, Numerical study of the dehydration and hydration processes of the Ca(OH)2/CaO system in an indirect-direct reactor, J. Energy Storage 71 (2023), 108119, https://doi.org/10.1016/j.est.2023.108119.
[29] C.P. Liu, S. Bai, L. Wang, Resistance forces on an intruder penetrating partially fluidized granular media, Phys. Rev. E 99 (2019), 012903, https://doi.org/10.1103/PhysRevE.99.012903.
[30] M.B. Stone, R. Barry, D.P. Bernstein, M.D. Pelc, Y.K. Tsui, P. Schiffer, Local jamming via penetration of a granular medium, Phys. Rev. E 70 (2004), 041301, https://doi.org/10.1103/PhysRevE.70.041301.
[31] W.C. Sung, J.Y. Kim, S.W. Chung, D.H. Lee, Effect of particle size distribution on hydrodynamics of pneumatic conveying system based on CPFD simulation, Adv. Powder Technol. 32 (2021) 2336–2344, https://doi.org/10.1016/j.apt.2021.05.010.
[32] H.Y. Xie, The role of interparticle forces in the fluidization of fine particles, Powder Technol. 94 (1997) 99–108, https://doi.org/10.1016/S0032-5910(97)03270-1.
[33] A. Castellanos, The relationship between attractive interparticle forces and bulk behaviour in dry and uncharged fine powders, Adv. Phys. 54 (2005) 263–376, https://doi.org/10.1080/17461390500402657.
[34] H. Rumpf, K. Sommer, K. Steier, Mechanismen der Haftkraftverstärkung bei der Partikelhaftung durch plastisches Verformen, Sintern und viskoelastisches Fließen, Chem. Ing. Tech. 48 (1976) 300–307, https://doi.org/10.1002/cite.330480408.
[35] J.N. Israelachvili, Chapter 13 - Van der Waals forces between particles and surfaces, in: J.N. Israelachvili (Ed.), Intermolecular and Surface Forces, Third edition, Academic Press, Boston, 2011, pp. 253–289, https://doi.org/10.1016/B978-0-12-391927-4.10013-1.
[36] M. Rostami Osanloo, K.A. Oyekan, W.G. Vandenberghe, A first-principles study on the electronic, thermodynamic and dielectric properties of monolayer ca(OH)2 and mg(OH)2, Nanomaterials. 12 (2022) 1774, https://doi.org/10.3390/nano12101774.
[37] M.A. Subramanian, R.D. Shannon, B.H.T. Chai, M.M. Abraham, M.C. Wintersgill, Dielectric constants of BeO, MgO, and CaO using the two-terminal method, Phys. Chem. Miner. 16 (1989) 741–746, https://doi.org/10.1007/BF00209695.
[38] A.F. Dunn, The dielectric constants of argon, carbon dioxide, nitrogen, and oxygen determined at an audio frequency, Can. J. Phys. 42 (1964) 1489–1498, https://doi.org/10.1139/p64-136.
[39] A. Michels, H. Lebesque, L. Lebesque, S.R. De Groot, Refractive index and Lorentz-Lorenz function of nitrogen up to 2000 atmospheres at 25°C, Physica. 13 (1947) 337–342, https://doi.org/10.1016/0031-8914(47)90006-2.
[40] C.J. Liu, E.F. Sieckmann, Refractive index of calcium oxide, J. Appl. Phys. 37 (1966) 2450–2452, https://doi.org/10.1063/1.1708835.
[41] S.S. Batsanov, E.D. Ruchkin, I.A. Poroshina, Refractive indices of elements and binary compounds, in: S.S. Batsanov, E.D. Ruchkin, I.A. Poroshina (Eds.), Refractive Indices of Solids, Springer, Singapore, 2016, pp. 33–41, https://doi.org/10.1007/978-981-10-0797-2_4.
[42] K.L. Johnson, K. Kendall, A.D. Roberts, D. Tabor, Surface energy and the contact of elastic solids, Proc. R. Soc. Lond. Math. Phys. Sci. 324 (1997) 301–313, https://doi.org/10.1098/rspa.1971.0141.
[43] S. Brunauer, D.L. Kantro, C.H. Weise, The surface energies of calcium oxide and calcium hydroxide, Can. J. Chem. 34 (1956) 729–742, https://doi.org/10.1139/v56-096.
[44] J.P. Seville, U. Tüzün, R. Clift, Processing of Particulate Solids, Springer Science & Business Media, 2012.
[45] H. Lu, X. Guo, Y. Jin, X. Gong, Effect of moisture on flowability of pulverized coal, Chem. Eng. Res. Des. 133 (2018) 326–334, https://doi.org/10.1016/j.cherd.2018.03.023.
[46] J. Cho, H.Y. Sohn, Effects of particle shape and size distribution on the overall fluid-solid reaction rates of particle assemblages, Can. J. Chem. Eng. 94 (2016) 1516–1523, https://doi.org/10.1002/cjce.22533.
[47] A. Irabien, J.R. Viguri, F. Cortabitarte, I. Ortiz, Thermal dehydration of calcium hydroxide. 2. Surface area evolution, Ind. Eng. Chem. Res. 29 (1990) 1606–1611, https://doi.org/10.1021/ie00104a005.
[48] S. Affleck, A.L. Thomas, A.F. Routh, N.M. Vriend, Novel protocol for quantifying powder cohesivity through fluidisation tests, Powder Technol. 415 (2023), 118147, https://doi.org/10.1016/j.powtec.2022.118147.